

Ultrafast Low-Temperature Crystallization of Solar Cell Graded Formamidinium-Cesium Mixed-Cation Lead Mixed-Halide Perovskites Using a Reproducible Microwave-Based Process

Maria João Brites,^{*,†} Maria Alexandra Barreiros,[†] Victoria Corregidor,[‡] Luis C. Alves,[§] Joana V. Pinto,^{||} Manuel J. Mendes,^{||} Elvira Fortunato,^{||} Rodrigo Martins,^{||} and João Mascarenhas[†]

[†]Laboratório Nacional de Energia e Geologia, LNEG/UER, Estrada do Paço do Lumiar, 22, 1649-038 Lisboa, Portugal

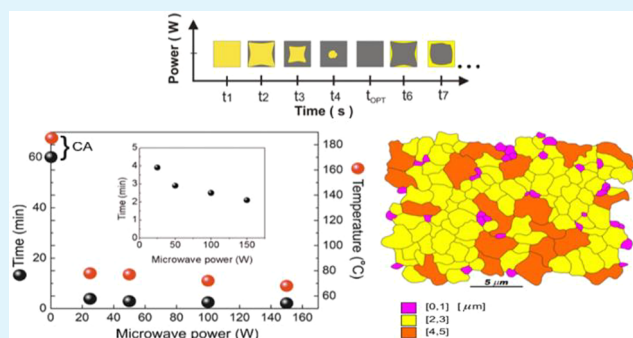
[‡]IPFN, Campus Tecnológico e Nuclear, Instituto Superior Técnico and [§]C2TN, Campus Tecnológico e Nuclear, Instituto Superior Técnico, Universidade de Lisboa, E. N.10, 2695-066 Bobadela LRS, Portugal

^{||}CENIMAT-I3N, Faculdade de Ciências e Tecnologia, Universidade Nova de Lisboa, Campus de Caparica, 2829-516 Caparica, Portugal

Supporting Information

ABSTRACT: The control of morphology and crystallinity of solution-processed perovskite thin-films for solar cells is the key for further enhancement of the devices' power conversion efficiency and stability. Improving crystallinity and increasing grain size of perovskite films is a proven way to boost the devices' performance and operational robustness, nevertheless this has only been achieved with high-temperature processes. Here, we present an unprecedented low-temperature (<80 °C) and ultrafast microwave (MW) annealing process to yield uniform, compact, and crystalline $\text{FA}_{0.83}\text{Cs}_{0.17}\text{Pb}(\text{I}_{1-x}\text{Br}_x)_3$ perovskite films with full coverage and micrometer-scale grains. We demonstrate that the nominal composition $\text{FA}_{0.83}\text{Cs}_{0.17}\text{PbI}_{1.8}\text{Br}_{1.2}$ perovskite films annealed at 100 W MW power present the same band gap, similar morphology, and crystallinity of conventionally annealed films, with the advantage of being produced at a lower temperature (below 80 °C vs 185 °C) and during a very short period of time (~2.5 min versus 60 min). These results open new avenues to fabricate band gap tunable perovskite films at low temperatures, which is of utmost importance for mechanically flexible perovskite cells and monolithic perovskite based tandem cells applications.

KEYWORDS: microwave annealing, fast low-temperature processing, micrometer-scale grains, mixed-cation lead mixed-halide perovskites, perovskite chemical composition



INTRODUCTION

Organo-metal halide perovskites have emerged as an extremely promising photovoltaic (PV) technology due to high power conversion efficiencies (PCE) and low fabrication cost. In a span of a few years, the record single-junction efficiency of perovskite solar cells has reached 22.7%¹ making it the most efficient solution-processed PV technology. Furthermore, their wide tunable band gap² makes perovskites highly attractive for use in tandem solar cells, that is, as top cells of narrower-band gap absorbers such as silicon (Si) and copper indium gallium selenide (CIGS).^{3–5}

One of the main challenges in the perovskite field is the fabrication of high quality films with controlled morphology, high surface coverage, and minimum pinholes.^{6,7} Factors such as charge dissociation efficiency, charge transport, and diffusion length of charge species are strongly dependent on the film crystallinity. Therefore, the control of the crystallization and thus the kinetics of film formation during deposition and

annealing are the key to boost the performance of solution-processed perovskite solar cells.^{8–11} For this purpose, approaches such as solvent engineering,¹² inclusion of additives into the precursor solution,^{13–17} substrate temperature,^{18,19} thermal annealing,²⁰ and solution-processed methods^{21–23} have been investigated by several research groups.

Recently, it has been shown that improvements in crystallinity and larger grain sizes can impact the stability of the perovskite film^{19,24,25} and several solution-processed approaches to achieve micrometer-sized perovskite grains have been reported.^{18,19} Usually, these approaches involve hot-casting of the perovskite precursor solution onto a substrate maintained above the crystallization temperature of the perovskite phase (that is, between 145 °C up to 180 °C

Received: November 19, 2018

Accepted: February 25, 2019

Published: February 25, 2019

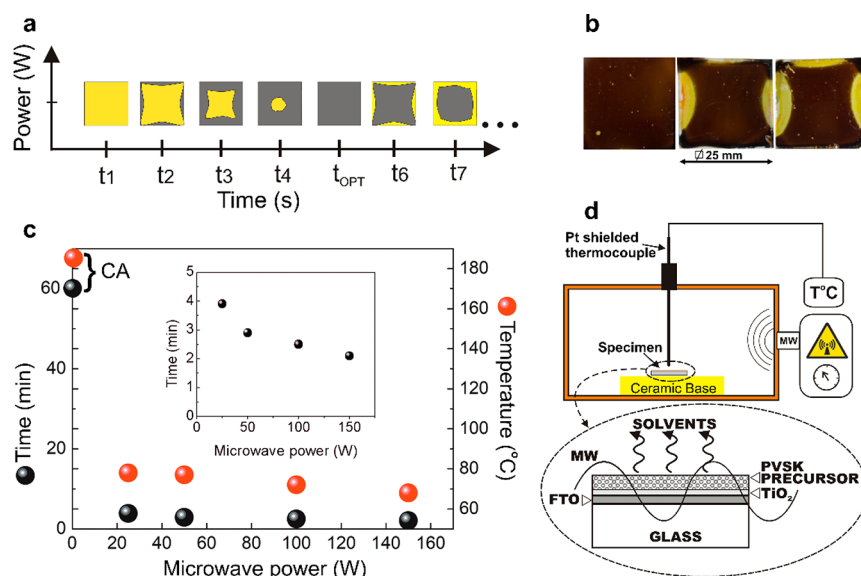


Figure 1. Microwave annealing of $\text{FA}_{0.83}\text{Cs}_{0.17}\text{PbI}_{1.8}\text{Br}_{1.2}$ perovskite. (a) Schematic representation of perovskite crystallization evolution with MW irradiation time (t). (b) Photograph of a perovskite film for $t = t_{\text{OPT}}$ (left photo), and $t > t_{\text{OPT}}$ (center and right photos) where visible degradation starts to occur from the edges. (c) Optimum MW irradiation time (t_{OPT}) (black) and maximum measured temperature at $t = t_{\text{OPT}}$ (red), as a function of MW power (inset: magnification on the range 0 to 5 min), compared with the CA time (60 min) and temperature (185 °C) of perovskite films with nominal composition $\text{FA}_{0.83}\text{Cs}_{0.17}\text{PbI}_{1.8}\text{Br}_{1.2}$ deposited on FTO/compact TiO_2 . (d) Schematic representation of perovskite MW annealing process.

depending on the perovskite chemical composition), which can extend the perovskite crystals growth, yielding large crystalline grains. Clearly, a lower temperature annealing process that allows full crystallization of the perovskite, keeping the morphological, structural, and optoelectronic quality of the films processed at higher temperatures, can be of major importance for the entire field of perovskite-based PV. In particular, it is crucial to enable novel device architectures such as perovskite tandem solar cells, and to allow integration in mechanically flexible substrates.^{26–28} In this context, microwave-driven annealing is a promising approach, as it is known that its processing temperature and time can be lower when compared to conventional thermal annealing.^{29,30}

Microwave heating uses the ability of some compounds (liquids or solids) to transform electromagnetic energy into heat (coupling at the molecular level).³¹ Energy transmission is produced by dielectric losses, and the magnitude of heating depends on the dielectric properties of the molecules, which means that the absorption of radiation and consequent heating may be performed selectively. In contrast to conventional heating (which is slow and relies on surface heating), microwave irradiation is rapid and volumetric, with the whole material heated simultaneously.³² In many processes of industrial interest, the volumetric heating provides significant reductions in the processing time and energy savings.

Mamun et al.³³ reported the use of microwave (MW) irradiation for rapid (≤ 8 min) and low temperature (≤ 260 °C) production of nanocrystalline titanium dioxide (nc- TiO_2) films with similar optical, morphological, and structural properties of the conventionally annealed films. The rapid fabrication time was not only attributed to direct absorption of MW energy by FTO coating in close contact with the TiO_2 film, allowing effective and efficient heat transfer from FTO to nc- TiO_2 , but also to the ability of organic molecules (solvent and binders present in the TiO_2 paste) to absorb MW radiation efficiently.

Recent studies related to MW annealing of methylammonium lead iodide perovskite films ($\text{CH}_3\text{NH}_3\text{PbI}_3$) show that this technique provides a fast and less energy-intensive process for the manufacture of perovskites,^{34,35} however under the conditions tested (fixed MW power and varying the irradiation time) no advantage was observed regarding the processing temperature (that is, the crystallization temperature of MW annealing at ~ 100 °C was similar to that of thermal annealing methods).

In this work, we report a versatile and ultrafast microwave (MW) annealing process to produce highly crystalline formamidinium–cesium mixed-cation lead mixed-halide perovskite films with micrometer-scale grains and preferred crystal orientation at low temperatures (< 80 °C) and processed at ambient atmosphere. Moreover, an innovative combined characterization toolset was developed to determine the real composition of mixed-cation lead mixed-halide perovskite films, showing that the stoichiometry can change with respect to the expected one (from the precursor solution preparation used). This is crucial for the fabrication of perovskite films with reproducible optoelectronic properties.

RESULTS AND DISCUSSION

Low-Temperature Crystallization of Mixed-Cation Lead Mixed-Halide Perovskite Films. Here we test the MW annealing process with state-of-art perovskites using formamidinium (FA) and cesium (Cs) mixed cation/iodide-bromide mixed anion perovskites formulations of nominal composition $\text{FA}_{0.83}\text{Cs}_{0.17}\text{PbI}_{1.8}\text{Br}_{1.2}$.³⁶ The selection of this wide-bandgap perovskite as test bed is based on its crystallization temperature (185 °C) and long crystallization time, improved photo-, moisture, and thermal stability, excellent optoelectronic properties (charge-carrier mobility exceeding $20 \text{ cm}^2 \text{ V}^{-1} \text{ s}^{-1}$) and its ideal band gap (~ 1.74 eV) for top subcells in double-junction tandem solar cells.^{10,11,36,37}

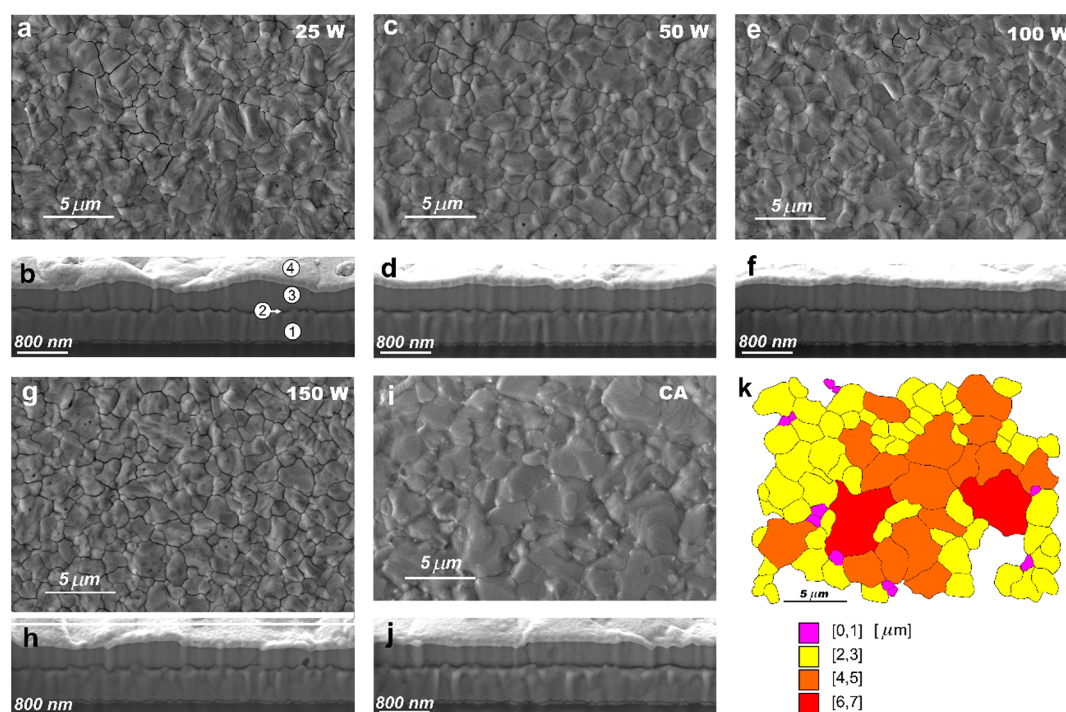


Figure 2. Characterization of nominal composition $\text{FA}_{0.83}\text{Cs}_{0.17}\text{PbI}_{1.8}\text{Br}_{1.2}$ perovskite films after different annealing conditions. The SEM analysis was performed with top-view images (upper ones) of the MW-perovskite films (a, 25 W; c, 50 W; e, 100 W; g, 150 W) and of the CA-perovskite film (i), as well as cross section images (bottom ones) of the same films (b, 25 W; d, 50 W; f, 100 W; h, 150 W; and j, CA). The layers indicated by the labels 1, 2, 3, and 4 in panel b correspond to FTO, compact TiO_2 , perovskite, and gold, respectively. (k) Grain boundary map of the CA-perovskite SEM image (i) obtained by digital image analysis, showing the different grain size classes.

The perovskite films with the nominal composition $\text{FA}_{0.83}\text{Cs}_{0.17}\text{PbI}_{1.8}\text{Br}_{1.2}$ were deposited on compact TiO_2 layer (prepared as described elsewhere³⁸) by spin coating a mixture of PbI_2 , PbBr_2 , FAI, and CsI in *N,N*-dimethylformamide (DMF) and using acidic additives (hydriodic acid, HI, and hydrobromic acid, HBr).^{11,36} Microwave annealing was performed at powers of 25, 50, 100, and 150 W, and the irradiation time (t_i) was set initially by visual check of the color change throughout the sample surface during the crystallization process, which allowed to estimate the irradiation time for each MW power. The estimated values were subsequently used and adjusted in the several MW-annealing tests, being complete crystallization of perovskite in every specimen confirmed by X-ray diffraction (XRD) (procedure described in Supporting Information, SI). The absence of PbI_2 peak in the diffractograms enabled to set the optimum irradiation time for each MW power.

For comparison sake, cycles in a conventional annealing (CA) oven were performed. The annealing program followed a multistep heating up to 185 °C with 60 min being the time from room temperature up to the end of the annealing plateau. In all cases, the films were annealed in ambient atmosphere.

In Figure 1a, we show a schematic representation of the perovskite crystallization evolution with MW irradiation time at a fixed power. The crystallization starts on the near-edge region and continues toward the sample's center. This is due to the edge effect that occurs when electromagnetic waves diffract on the specimen's edge, rising locally the temperature, and consequently starting the crystallization on that site.³⁹ The magnitude of the specific heating power depends on the polarization and propagation direction of the incident electromagnetic waves. The spatial nonuniformity of the

absorbed power is noticeable when the wave vector is parallel to the sample surface but perpendicular to the sample edge.

This edge effect can be overcome with the use of a shield for the incident waves, that is, aluminum thin sheet (10 μm), positioned around the sample edges to attenuate the MW radiation, leading to an improvement of the temperature uniformity of the sample.³⁹ The consideration of the MW penetration depth into a material is of great significance to an efficient and uniform MW heating process. In order to have the whole material coupling with MW, the sample's dimension should be comparable to the penetration depth, so that the entire sample can be irradiated by MW radiation to get the maximal heating rate. In the present case, the stack thickness ($\sim 1 \mu\text{m}$) of FTO, TiO_2 , and as-deposited perovskite film is within the dimension of the respective MW penetration depth (DMF penetration depth is 0.46 cm⁴⁰), allowing the materials to be heated by direct microwave dielectric heating.

For each MW power, there is an optimum irradiation time (t_{OPT}) (Figure 1b, left photo), after which perovskite degradation begins to occur, also starting from the edges toward the sample center (as shown in Figure 1b, center and right photos). As expected, t_{OPT} decreases from 4 to 2 min with the increase of MW power (Figure 1c), and for all the MW powers tested the perovskite crystallization occurs at a temperature below 80 °C.

In Figure 1d, a schematic representation of the perovskite MW annealing process is shown. The residual polar solvent (DMF) present in the as-deposit perovskite film absorbs MW energy due to its high dielectric constant ($\epsilon = 37.51$ at 25 °C). The DMF's dipoles are sensitive to external electric fields and will attempt to align themselves with the field by rotation. At the used frequency, 2.45 GHz, the dipoles do not have enough

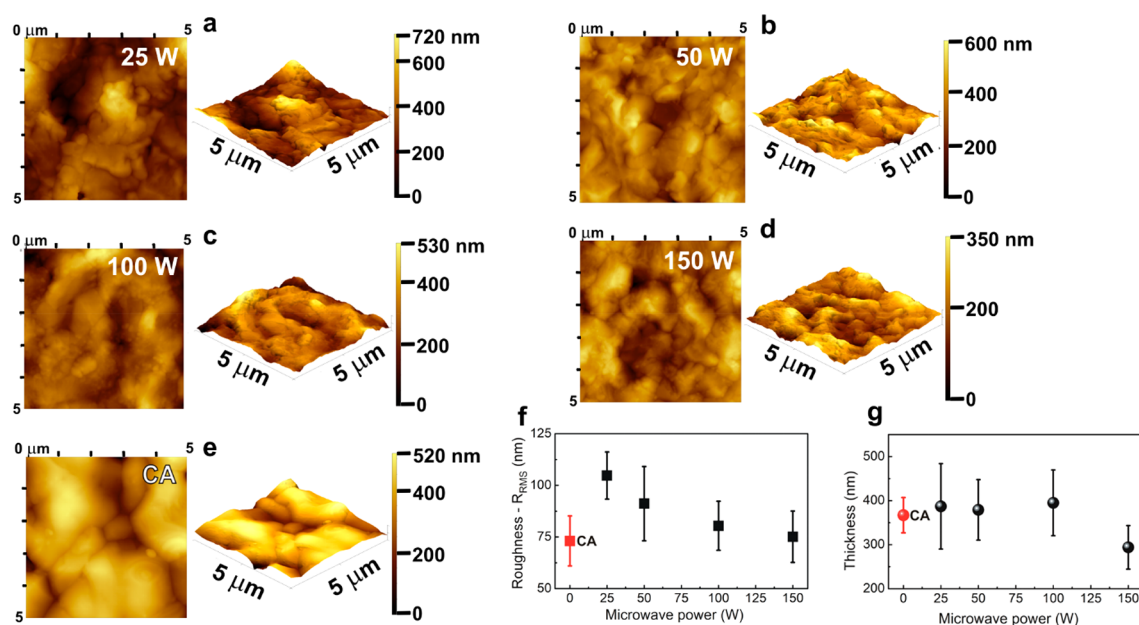


Figure 3. AFM images ($5 \times 5 \mu\text{m}^2$) of nominal composition $\text{FA}_{0.83}\text{Cs}_{0.17}\text{PbI}_{1.8}\text{Br}_{1.2}$ perovskite films after different annealing conditions (a, 25 W; b, 50 W; c, 100 W; d, 150 W; and e, CA) in an area of $5 \times 5 \mu\text{m}^2$. (f) R_{RMS} (average of 3 different film regions) and (g) thickness (average of 10 measurements by SEM-FIB cross section analysis) of CA- and MW-perovskite films as a function of MW power. The error bars represent the standard deviation from the mean.

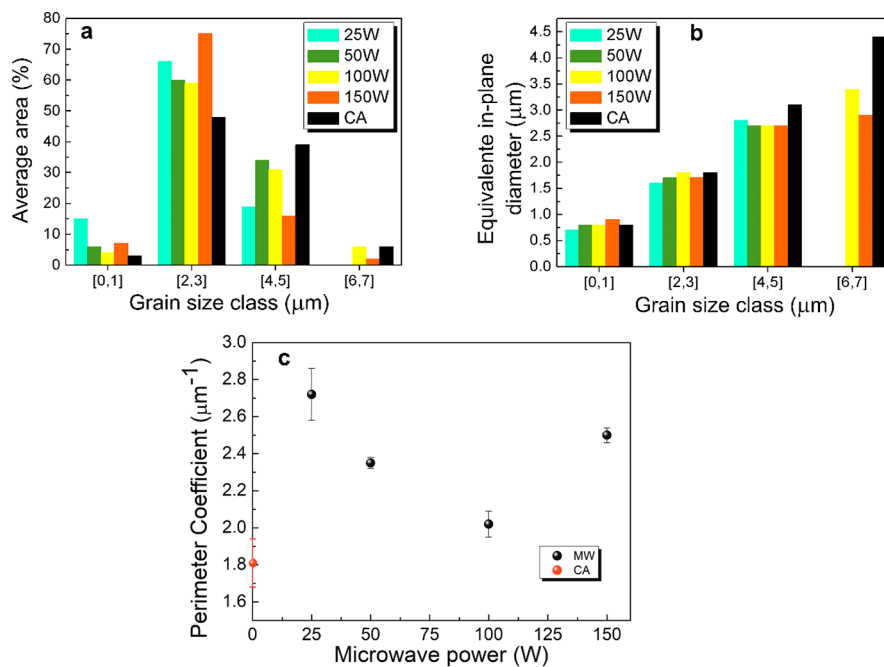


Figure 4. Digital image analysis of the perovskite grain size. (a) Average area percentage of each grain size class and (b) equivalent in-plane diameter of the grains in CA- and MW-perovskite films for each grain size class. (c) Perimeter coefficient of the grains in CA- and MW-perovskite films as a function of MW power.

time to be constantly aligned to the oscillating field, colliding with one another, and the power is dissipated by heat generation in the material. This MW heating will promote the quick evaporation of the solvent and consequently the crystallization of perovskite material. The constituents of the substrate, that is, FTO and TiO_2 , have also their own contribution to MW heating. The TiO_2 showed moderate coupling to microwaves because it is a stoichiometric semiconductor having both low electrical conductivity and

low magnetic induction loss.⁴¹ On the other hand, knowing that FTO is a nonstoichiometric semiconductor with high electrical conductivity, material-MW coupling is possibly correlated with high concentration of conduction electrons and the temperature rise attributed to induction losses from electron conduction. The two mentioned MW heating mechanisms, that is, dipolar polarization and conductive mechanisms, work together and are responsible for the rapid,

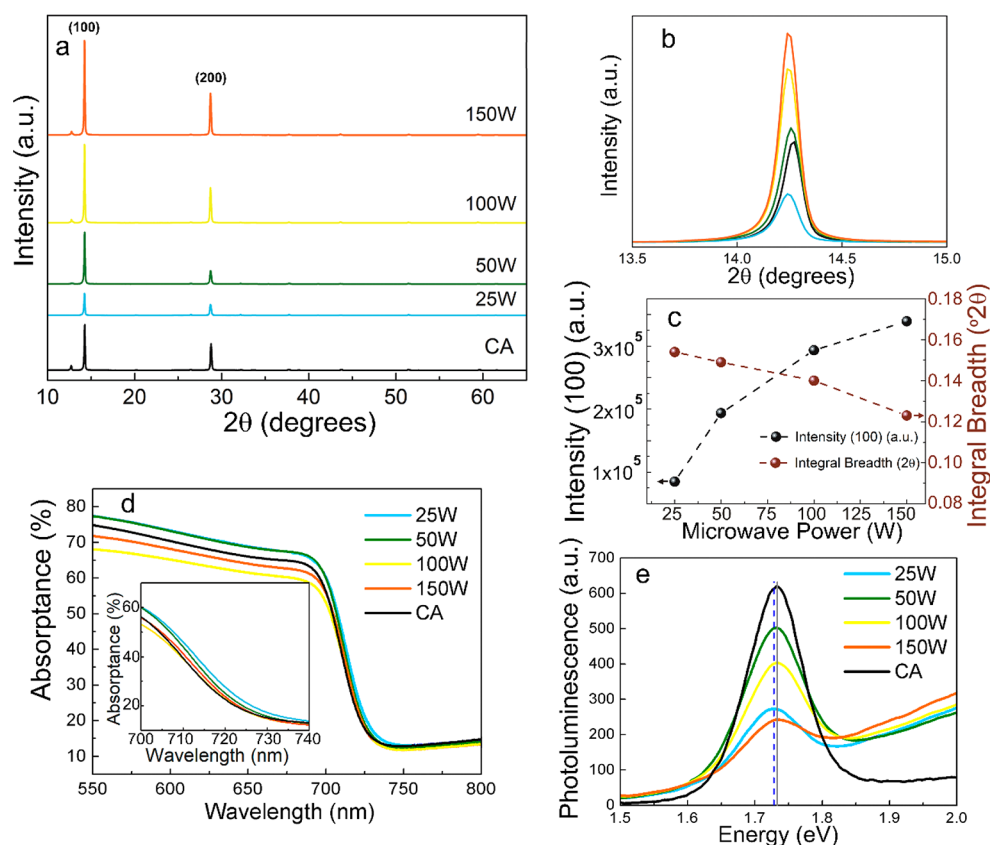


Figure 5. Structural and optical characterization of nominal composition $\text{FA}_{0.83}\text{Cs}_{0.17}\text{PbI}_{1.8}\text{Br}_{1.2}$ perovskite films deposited on FTO/compact TiO_2 substrates. (a) XRD patterns for CA- and MW-perovskite films. (b) Detail of the XRD patterns of the films for 2θ from 13° to 15° . (c) Intensity and integral breadth ($^\circ 2\theta$) of the (100) diffraction peak as a function of MW power. (d) UV-vis absorbance spectra (inset: magnification on the range 700 to 740 nm) and (e) steady-state photoluminescence (PL) spectra.

low-temperature and controllable crystallization of perovskites films.

The top-view and cross section scanning electron microscope (SEM) images for each MW- and CA-perovskite films are shown in Figure 2a–j. To evaluate the uniformity of surface morphology of each MW- and CA-perovskite films, five different regions (an area of approximately 2 cm^2 in the center of each sample) were chosen randomly to obtain SEM images at low magnification ($5000\times$). Figure S2 exemplifies the surface uniformity assessment for the 100 W perovskite film.

All perovskite films are compact and pinhole-free, which is highly desirable for efficient perovskite solar cell fabrication. As displayed in the cross-section SEM images (Figure 2d,f,h,j), perovskite films annealed at 50, 100, and 150 W MW power and conventionally annealed films show a uniform thickness (around 379, 395, 294, and 367 nm, respectively). At 25 W MW power, a significant film thickness variability is observed (Figure 2b, thickness variation between 270 and 565 nm), being the thickness average of 387 nm. The thickness decrease of the perovskite film annealed at 150 W is due to the degradation of the film, that is, loss of mass associated with the organic cation, which is confirmed by the appearance of the peak of PbI_2 at $2\theta \sim 12.7^\circ$ in the XRD pattern (X-ray diffraction analysis of MW- and CA-perovskite films is discussed later).

Top-view and 3D atomic force microscopy (AFM) images for each MW- and CA-perovskite films are shown in Figure 3a–e. The root-mean-square surface roughness (R_{RMS}) of the perovskite films was found to decrease with the increase of

MW power (Figure 3f). Compared to the CA-perovskite film ($R_{\text{RMS}} = 73.1 \text{ nm}$), the 100 W processed specimens showed a slightly higher R_{RMS} (80.4 nm), while the 150 W ones showed a similar value (75.1 nm).

To help establish the relationship between MW power and grain size of the MW-perovskite films, we studied the mean dimensions of the grains in the films, namely the equivalent in-plane diameter, average area, and perimeter coefficient (ratio between the total perimeter and the total area of the grains), determined by a digital image analysis in-house procedure (Figure 4) described in Supporting Information (SI).

As shown in Figure 4a, for the perovskite films processed at 25, 50, and 100 W, the average area of the [0,1] and [2,3] grain size classes (that is, the classes with smaller grain sizes) decreases with increasing power. On the other hand, the average area of the [4,5] and [6,7] classes seems to increase with MW power, being this at the expense of the immediately preceding grain size class, that is, larger grains grow at the expense of smaller ones (Ostwald ripening).⁴² These findings are more noticeable in perovskite films processed at 100 W. In fact, the average area of the [0,1] class decreases from 15% to 4% when the MW power is increased from 25 to 100 W, and at the same time the average area of the [4,5] and [6,7] grain size class increases from 19% to 31% and from 0% to 6%, respectively. As shown in Figure 4b, the equivalent in-plane diameter is approximately constant within each grain size class for all the specimens, regardless of the MW power used. On the other hand, regarding the values of the perimeter coefficient calculated for each specimen, Figure 4c, there is a

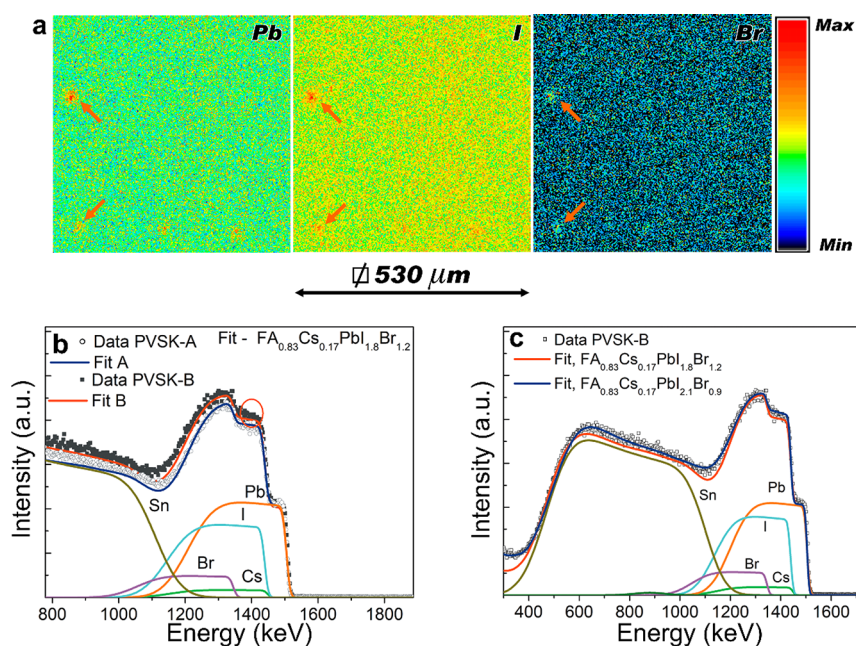


Figure 6. Elemental analysis and depth profile of CA perovskite films. (a) The 2 MeV H^+ 2D-PIXE elemental distribution maps of PVSK-A for Pb (left), I (middle), and Br (right). Red arrows indicate local heterogeneities; (b) 1.6 MeV He^+ RBS experimental data and fits of PVSK-A (open gray circles and blue line) and PVSK-B (black squares and red line) films (elemental contributions to the fits are also shown), using nominal composition. The difference between film thicknesses is given by the different widths of the spectra. The red circle marks an underestimation of I content. (c) The 1.6 MeV He^+ RBS data (open circles) and fits assuming nominal composition (red line) or composition obtained from PIXE (blue line) for PVSK-B. Also shown are the individual elemental contributions for the blue line fit.

decreasing trend as the MW power increases from 25 to 100 W, due to the increase in the particle size and consequent decrease in the total particles perimeter (see digital image analysis procedure in SI). However, this trend changes for the specimens processed at 150 W, as such high power seems to go beyond the maximum balanced MW power for the annealing of this type of perovskite. Therefore, it is preferential to MW-anneal the perovskite films at applied powers around 100 W, yielding a similar perimeter coefficient value to that of CA-perovskite films, and presenting an equivalent morphology.

To understand the impact of MW annealing on the formation and crystallization of perovskite phases, we performed XRD measurements on the perovskite films (see procedure describe in SI). As presented in Figure 5a, all XRD patterns show high intensity peaks, corresponding to the (100) and (200) reflections from characteristic planes of the cubic perovskite, indicating a highly preferred orientation along these directions. In Figure 5b, we show the XRD pattern zoomed around the (100) peak of perovskite films at $2\theta \sim 14.25^\circ$, processed at 50, 100, and 150 W MW power and for CA films.

In the case of 25 W-perovskite films, a small shift to lower angles is observed ($2\theta \sim 14.23^\circ$) for the (100) peak (Figure 5b) when compared with the other MW annealed samples, suggesting a perovskite composition with higher content of iodine.^{10,36} Peak profile deconvolution was used to assess the $K\alpha_1$ peak position. From Figure 5c, we observe that the intensity of the peaks increases with increasing MW power, and the integral breadth values of the (100) peak decrease with increasing MW power, indicating a higher crystallinity in the samples annealed at higher power.

The absorbance spectra of CA and MW-perovskite films exhibit comparable optical properties with a strong absorption in the range of 550–700 nm, as shown in Figure 5d. From the absorption profile, a slight red-shift of the band edge is visible

for the 25 W-perovskite. The band gap energy (E_g) was estimated from the reflectance measurements by applying the modified Kubelka–Munk ($F(R)$) method using the equation: $F(R) = (1 - R)^2/2R$ and plotting $(F(R) \times h\nu)^2$, as a function of the photon energy ($h\nu$) in eV, where R is the reflectance, h is the Planck's constant (J·s), and ν is the light frequency (s^{-1}).⁴³ An E_g of ~ 1.72 eV was obtained for CA and MW-perovskite films (Figure S1 of SI), with the exception of the 25 W-perovskite that shows a slightly lower band gap (E_g 1.71 eV), indicating a slightly higher content of iodine in the perovskite's composition.³⁶ This band gap shift was also detected using the photoluminescence (PL) emission spectra, as presented in Figure 5e. The slight red-shift of the band edge observed in the absorbance spectra of 25 W-perovskite film and the lower band gap value obtained ($E_g = 1.71$ eV) are also in agreement with the small shift to lower angles observed ($2\theta \sim 14.23^\circ$) for the (100) peak in the XRD pattern (Figure 5b).

It is noteworthy that the perovskite films annealed at 100 W microwave power present the same band gap ($E_g = 1.72$ eV) and similar morphology and crystallinity of conventionally annealed films, with the advantage of being produced at a lower temperature (below 80 °C vs 185 °C) and during a very short period of time (~ 2.5 min vs 60 min). As demonstrated here, the ultrafast MW annealing process not only entails a low temperature fabrication of full coverage, crystalline perovskite films with micrometer-scale grains and preferred crystal orientations, but also allows simultaneously improving crystallinity and increasing grain size, through optimization of MW settings, such as power and irradiation time.

Perovskite Chemical Composition upon Crystallization. The estimated band gap values of both MW (100 W) and CA $FA_{0.83}Cs_{0.17}PbI_{1.8}Br_{1.2}$ films ($E_g = 1.72$ eV for both films) are lower than the previous reported band gap ($E_g = 1.74$ eV) for this particular nominal composition.³⁶ This can be

Table 1. EDS and PIXE Analysis of Pb, I, and Br in Perovskites PVSK-A and PVSK-B^a

sample	E_g (eV)	PIXE atomic fraction			EDS atomic fraction		
		I	Br	I/Br	I	Br	I/Br
PVSK-A	1.74	2.02 ± 0.08	0.98 ± 0.02	2.0	1.99 ± 0.09	0.95 ± 0.04	2.0
PVSK-B	1.73	2.14 ± 0.03	0.91 ± 0.03	2.3	2.0 ± 0.2	0.9 ± 0.1	2.2

^aThe results are expressed in atomic fraction normalized to the Pb content.

attributed to the fact that the perovskite chemical composition in the fabricated films may differ from that which is estimated upon mixing the perovskite precursor compounds in the precursor solution. Therefore, we set out to investigate this aspect, as it is of major relevance for all perovskite applications.

To this end, we used ion beam analysis (IBA) techniques⁴⁴ to assess the lateral and in-depth elemental composition of the perovskite films (see SI) by means of 2D particle induced X-ray emission (2D-PIXE) maps⁴⁵ and Rutherford backscattering spectrometry (RBS)⁴⁶ following the total IBA approach.⁴⁴

For this study, two sets of five conventionally annealed perovskite films³⁶ were prepared from two independent perovskite precursor solutions (solution A and B) with nominal composition $\text{FA}_{0.83}\text{Cs}_{0.17}\text{PbI}_{1.8}\text{Br}_{1.2}$, and the band gap was determined for all films based on diffuse reflectance measurements, as described previously (Table S1). Two films were then selected, one from each precursor solution (solution A and B), that presented a band gap similar to that previously reported in the literature for this particular nominal composition³⁶ (Figure S3). IBA measurements were carried out on the selected films, referred here as PVSK-A ($E_g = 1.74$ eV) and PVSK-B ($E_g = 1.73$ eV) (Table S1 and Figure S3), which were also characterized by SEM, energy dispersive spectrometry (EDS), digital image analysis and XRD techniques (see Figures S4–S6 and Table S2).

For illustration, Figure 6a shows the 2D-PIXE elemental distribution maps obtained for PVSK-A using a 2 MeV proton beam (equivalent maps for PVSK-B are presented in Figure S7).

The multielemental distribution over the surface presents a quite large uniform area, pointing toward an overall homogeneous chemical composition of the film. Small local heterogeneities can be observed (red arrows), concerning regions of higher intensity for the three elements shown, that were found to be related to thicker perovskite crystals.

From similar maps obtained for the PVSK-A and PVSK-B films, three homogeneous areas ($\sim 90 \times 90 \mu\text{m}^2$) were chosen to simultaneously record the PIXE and RBS spectra. PIXE and EDS results of Pb, I, and Br are expressed in atomic fraction normalized to the Pb content (Table 1). Although probing different sample depths (that is, the entire material layer is probed by the 2 MeV proton beam, whereas EDS information is gathered over a shallow sample depth), and despite the higher uncertainty of EDS, the results are consistent. PIXE and EDS provided similar Br values, indicating a chemical composition different from the nominal one ($\text{FA}_{0.83}\text{Cs}_{0.17}\text{PbI}_{1.8}\text{Br}_{1.2}$) and still different between PVSK-A and PVSK-B films, as expected.

Although the band gap value of PVSK-A is consistent with previous reports,³⁶ the I/Br ratio obtained is higher than that of the precursor perovskite solution (I/Br ratio 1.5), corresponding to a real composition in the film of $\text{FA}_{0.83}\text{Cs}_{0.17}\text{PbI}_{2.0}\text{Br}_{1.0}$. As shown in Figure S6, the PVSK-A XRD pattern exhibits the two characteristic peaks of perovskite at 14.31° and 28.84° which are assigned to the (100) and

(200) crystal planes, respectively. The slight variation in chemical composition of PVSK-A and PVSK-B films is in accordance with XRD results (Table S2) and with the different measured band gaps (Figure S3), since lower Br content in the perovskite chemical composition decreases the band gap and shifts the diffraction peaks to lower 2θ values.^{10,36}

Figure 6b shows the RBS experimental spectra obtained for PVSK-A and PVSK-B, using 1.6 MeV alpha beam together with the best fits, considering the following: (a) a single layer of perovskite with the nominal composition $\text{FA}_{0.83}\text{Cs}_{0.17}\text{PbI}_{1.8}\text{Br}_{1.2}$, followed by a TiO_2 compact layer, a F-doped SnO_2 (FTO) and glass layers and (b) the interface roughness to increase the energy spread resolution as a function of depth.⁴⁷

The RBS results show that a single layer of perovskite is enough to achieve good fits, indicating an in-depth uniform material composition which contrasts to that previously found for MAPbI_3 perovskites.⁴⁸ Moreover, the different width of the Cs, Br, I, and Pb signals observed in the RBS spectra correspond to an $\sim 4\%$ thickness difference between PVSK-A and PVSK-B films (2434×10^{15} and 2534×10^{15} at/cm², respectively). Also comparing the fit curves with experimental data it is noticeable that the I surface barrier height (proportional to the I content) is slightly underestimated, being this difference more evident for PVSK-B (red circle in Figure 6b). This finding indicates the need to consider a higher value of I in the perovskite film to achieve a better fit, which is in agreement with PIXE results (Table 1).

As shown in Figure 6c, for PVSK-B, when considering a single layer of perovskite with the chemical composition obtained by PIXE ($\text{FA}_{0.83}\text{Cs}_{0.17}\text{PbI}_{2.1}\text{Br}_{0.9}$), the corresponding RBS fit (blue line) displays a closer agreement with the experimental data than that obtained for the nominal composition (red line). Using the same approach for PVSK-A films (Figure S8), a better RBS fit was also achieved considering the chemical composition obtained by PIXE analysis ($\text{FA}_{0.83}\text{Cs}_{0.17}\text{PbI}_{2.0}\text{Br}_{1.0}$). These results show that through a total IBA approach it is possible to set and measure the difference between the real composition of the crystallized perovskite and the nominal content in its precursor solution, confirming at the same time the perovskite in-depth composition uniformity.

This study demonstrates that $\text{FA}_{0.83}\text{Cs}_{0.17}\text{PbI}_{1.8}\text{Br}_{1.2}$ perovskite precursor solution, prepared as previously reported,³⁶ crystallizes with a Br content lower than the nominal value with an in-depth uniform composition. Moreover, it was found that the PVSK-A ($E_g = 1.74$ eV) and PVSK-B ($E_g = 1.73$ eV) have the real composition of $\text{FA}_{0.83}\text{Cs}_{0.17}\text{PbI}_{2.0}\text{Br}_{1.0}$ and $\text{FA}_{0.83}\text{Cs}_{0.17}\text{PbI}_{2.1}\text{Br}_{0.9}$, respectively, being the slight difference of the band gap of these films in accordance with variations of Br content in the chemical composition of the perovskite that occur during its self-organization upon crystallization.

CONCLUSIONS

In summary, we have demonstrated that microwave annealing process is an efficient and ultrafast method for low-temperature fabrication of compact, pinhole-free, and highly crystalline formamidinium–cesium mixed-cation lead mixed-halide perovskite films with micrometer-scale grains and preferred crystal orientation. It was also found that the improvement in crystallinity and enhancement in perovskite grain sizes can be achieved by optimization of microwave output power and irradiation time. Perovskite films prepared from $\text{FA}_{0.83}\text{Cs}_{0.17}\text{PbI}_{1.8}\text{Br}_{1.2}$ precursor solution and annealed at 100 W microwave power present the same band gap, similar morphology, and crystallinity of conventionally annealed films. Moreover, the used IBA techniques allowed establishing the dependence of band gap variation of the perovskite films with the changes in the perovskite chemical composition upon the crystallization process. This work is the first to show that mixed-cation mixed-halide $\text{FA}_{0.83}\text{Cs}_{0.17}\text{Pb}(\text{I}_{(1-x)}\text{Br}_x)_3$ perovskite with an optical band gap of ~ 1.74 eV has the real composition of $\text{FA}_{0.83}\text{Cs}_{0.17}\text{PbI}_2\text{Br}$.

In view of photovoltaic applications, the perovskite films analyzed here were formed on glass substrates coated with the typical *n*-contact layers (FTO/compact TiO_2) of state-of-the-art perovskite solar cells composed of the conventional superstrate device architecture. As demonstrated here, microwave annealing opens new avenues to fabricate band gap tunable perovskite films at low temperatures, which is of utmost importance for their integration in mechanically flexible perovskite cells and/or monolithic perovskite based tandem cells.

EXPERIMENTAL SECTION

Materials. Cesium iodide (CsI, 99.9%), lead(II) bromide (PbBr_2 , 98%), lead(II) iodide (PbI_2 , 99%), and hydrobromic acid (HBr, 48 wt %) were purchased from Sigma-Aldrich, and hydriodic acid (HI, 57 wt %) was purchased from Alfa Aesar. All chemicals were used as received without further purification.

Perovskite Precursor Solution. The perovskite precursor solution (0.95 M) with nominal composition of $\text{FA}_{0.83}\text{Cs}_{0.17}\text{PbI}_{(0.6}\text{Br}_{0.4})_3$ was prepared by dissolving FAI (272 mg), CsI (83.4 mg), PbI_2 (350 mg), and PbBr_2 (418 mg) in *N,N*-dimethylformamide (2 mL). HI (109.4 μL) and 54.6 μL HBr were added and the solution was stirred for 48 h at room temperature.

Perovskite Film Preparation. The compact TiO_2 layer (c- TiO_2) was coated onto an F-doped SnO_2 (FTO, Pilkington, TEC8) substrate by spin coating a 0.15 M titanium diisopropoxide bis(acetylacetonate) in 1-butanol, at 2000 rpm for 20 s.³⁶ The c- TiO_2 films were annealed at 500 °C, for 30 min. The perovskite precursor solutions were filtered with 0.20 μm PTFE filters and spin-coated at 2000 rpm for 45 s on a c- TiO_2 /FTO substrate preheated at 70 °C. The films were dried on a hot plate at 70 °C for 5 min, and then annealed in a microwave oven at different power levels, or in a conventional oven in air atmosphere following a multistep temperature ramp up to 185 °C (room temperature, 10 °C/min; 100 °C, 10 min, 10 °C/min; 185 °C, 30 min).

Microwave Annealing of Perovskite Films. The microwave annealing tests were performed in a Microwave Research Applications Inc. U.S.A. oven with multimodal cavity, 1 kW nominal power, and 2.45 GHz frequency magnetron. During irradiation, temperatures were measured by a platinum shielded type-S thermocouple placed 2 mm above the specimens. At the end of the MW cycle, temperatures were measured by an external thermocouple in contact with the samples. All the annealing tests were performed in air at microwave power of 25, 50, 100, and 150 W.

Perovskite Film Characterization. SEM was performed on a Philips XL30 FEG (field emission electron source). SEM secondary

electron top-view images were obtained at an acceleration voltage of 10 kV. For this study, the samples were not coated with any conductive surface layer. Semiquantitative elemental composition was obtained with an EDS (EDAX) system equipped with a Si(Li) detector and a 3 μm super ultrathin window (SUTW). Spectra were collected at an acceleration voltage of 30 kV for 300 s acquisition time. The same samples analyzed by SEM were gold-coated to obtain cross section images with the Zeiss Auriga CrossBeam system, and the cross section was done by focused ion beam (FIB) milling with the Ga liquid metal ion source (LMIS) at 30 kV acceleration voltage. SEM imaging was done at 5 kV acceleration voltage of the electron beam. AFM analysis was performed using an Asylum Research MFP-3D Stand Alone AFM system. Measurements were performed in tapping (alternate contact) mode in air, using commercially available silicon AFM probes (Olympus AC160TS; $k = 26$ N/m; $f_0 = 300$ kHz). AFM topography images ($5 \times 5 \mu\text{m}^2$) were obtained in three different zones with a minimum resolution of 256×1024 points and in an area of approximately 1 mm^2 . The XRD patterns were recorded using a Panalytical MPD XPert Pro diffractometer in Bragg–Brentano configuration and using a $\text{CuK}\alpha$ radiation source. The data were collected using a X'Celerator 1D detector with a step size of 0.02° and was analyzed with HighScore plus Software. The total transmittance (*T*) and reflectance (*R*) spectra of perovskite films were acquired using an ultraviolet–visible–near double beam infrared spectrophotometer (PerkinElmer Lambda 950) equipped with an integrating sphere. Steady-state photoluminescence was measured using a PerkinElmer LS 55 fluorescence spectrometer with a xenon flash lamp as the luminous source. An excitation wavelength of 400 nm was used for all samples. The emission spectra were measured from 600 to 900 nm in steps of 1 nm and with the scanning speed of 100 nm/min.

ASSOCIATED CONTENT

Supporting Information

The Supporting Information is available free of charge on the ACS Publications website at DOI: 10.1021/acsaem.8b02005.

Tauc plots, scanning electron microscope images, X-ray diffraction patterns, 2D-PIXE elemental distribution maps, and RBS data of perovskite films; details on the digital image analysis method and IBA techniques. (PDF)

AUTHOR INFORMATION

Corresponding Author

*E-mail: mjoao.brites@lneg.pt.

ORCID

Maria João Brites: 0000-0002-1081-7191

Joana V. Pinto: 0000-0003-0847-7711

Manuel J. Mendes: 0000-0002-7374-0726

Elvira Fortunato: 0000-0002-4202-7047

Notes

The authors declare no competing financial interest.

ACKNOWLEDGMENTS

This work was supported by National Funds through FCT, Foundation for Science and Technology, under the projects ALTALUZ (PTDC/CTM-ENE/5125/2014) and SUPER-SOLAR (PTDC/NAN-OPT/28430/2017) and partially by FEDER funds through the COMPETE 2020 Program under the project UID/CTM/50025/2013. M.J.M. also acknowledges funding by FCT through the Grant SFRH/BPD/115566/2016. V.C. and L.C.A. acknowledge FCT funding support through projects UID/FIS/50010/2013 and UID/Multi/04349/2013, respectively. The authors would like to thank Dr. Daniela Gomes and Dr. Tomás Calmeiro for

assistance with SEM-FIB and AFM analysis, respectively. The authors would like to thank Pilkington for supplying free samples of FTO-TEC8.

REFERENCES

- (1) <https://www.nrel.gov/pv/assets/pdfs/pv-efficiency-chart.pdf>, 03–01–2019, NREL Photovoltaic Research, <http://www.nrel.gov>.
- (2) Noh, J. H.; Im, S. H.; Heo, J. H.; Mandal, T. N.; Seok, S., II Chemical Management for Colorful, Efficient, and Stable Inorganic-Organic Hybrid Nanostructured Solar Cells. *Nano Lett.* **2013**, *13* (4), 1764–1769.
- (3) Wu, Y.; Yan, D.; Peng, J.; Duong, T.; Wan, Y.; Phang, S. P.; Shen, H.; Wu, N.; Barugkin, C.; Fu, X.; et al. Monolithic Perovskite/Silicon-Homojunction Tandem Solar Cell with over 22% Efficiency. *Energy Environ. Sci.* **2017**, *10* (11), 2472–2479.
- (4) Duong, T.; Wu, Y. L.; Shen, H.; Peng, J.; Fu, X.; Jacobs, D.; Wang, E. C.; Kho, T. C.; Fong, K. C.; Stocks, M.; et al. Rubidium Multication Perovskite with Optimized Bandgap for Perovskite-Silicon Tandem with over 26% Efficiency. *Adv. Energy Mater.* **2017**, *7* (14), 1–11.
- (5) Shen, H.; Duong, T.; Peng, J.; Jacobs, D.; Wu, N.; Gong, J.; Wu, Y.; Karuturi, S. K.; Fu, X.; Weber, K.; et al. Mechanically-Stacked Perovskite/CIGS Tandem Solar Cells with Efficiency of 23.9% and Reduced Oxygen Sensitivity. *Energy Environ. Sci.* **2018**, *11* (2), 394–406.
- (6) Ball, J. M.; Petrozza, A. Defects in Perovskite-Halides and Their Effects in Solar Cells. *Nature Energy* **2016**, *1* (11), 16149.
- (7) Dubey, A.; Adhikari, N.; Mabrouk, S.; Wu, F.; Chen, K.; et al. A Strategic Review on Processing Routes towards Highly Efficient Perovskite Solar Cells. *J. Mater. Chem. A* **2018**, *6*, 2406–2431.
- (8) Eperon, G. E.; Burlakov, V. M.; Docampo, P.; Goriely, A.; Snaith, H. J. Morphological Control for High Performance, Solution-Processed Planar Heterojunction Perovskite Solar Cells. *Adv. Funct. Mater.* **2014**, *24* (1), 151–157.
- (9) Xing, G.; Mathews, N.; Sun, S.; Lim, S. S.; Lam, Y. M.; Grätzel, M.; Mhaisalkar, S.; Sum, T. C. Long-Range Balanced Electron-and Hole-Transport Lengths in Organic-Inorganic $\text{CH}_3\text{NH}_3\text{PbI}_3$. *Science* **2013**, *342* (6156), 344–347.
- (10) Rehman, W.; McMeekin, D. P.; Patel, J. B.; Milot, R. L.; Johnston, M. B.; Snaith, H. J.; Herz, L. M. Photovoltaic Mixed-Cation Lead Mixed-Halide Perovskites: Links between Crystallinity, Photo-Stability and Electronic Properties. *Energy Environ. Sci.* **2017**, *10* (1), 361–369.
- (11) McMeekin, D. P.; Wang, Z.; Rehman, W.; Pulvirenti, F.; Patel, J. B.; Noel, N. K.; Johnston, M. B.; Marder, S. R.; Herz, L. M.; Snaith, H. J. Crystallization Kinetics and Morphology Control of Formamidinium–Cesium Mixed-Cation Lead Mixed-Halide Perovskite via Tunability of the Colloidal Precursor Solution. *Adv. Mater.* **2017**, *29* (29), 1607039.
- (12) Jeon, N. J.; Noh, J. H.; Kim, Y. C.; Yang, W. S.; Ryu, S.; Seok, S., II Solvent Engineering for High-Performance Inorganic-Organic Hybrid Perovskite Solar Cells. *Nat. Mater.* **2014**, *13* (9), 897–903.
- (13) Pan, J.; Mu, C.; Li, Q.; Li, W.; Ma, D.; Xu, D. Room-Temperature, Hydrochloride-Assisted, One-Step Deposition for Highly Efficient and Air-Stable Perovskite Solar Cells. *Adv. Mater.* **2016**, *28*, 8309–8314.
- (14) Yang, L.; Wang, J.; Leung, W. W. F. Lead Iodide Thin Film Crystallization Control for High-Performance and Stable Solution-Processed Perovskite Solar Cells. *ACS Appl. Mater. Interfaces* **2015**, *7* (27), 14614–14619.
- (15) Sun, Y.; Peng, J.; Chen, Y.; Yao, Y.; Liang, Z. Triple-Cation Mixed-Halide Perovskites: Towards Efficient, Annealing-Free and Air-Stable Solar Cells Enabled by $\text{Pb}(\text{SCN})_2$ Additive. *Sci. Rep.* **2017**, *7*, 1–7.
- (16) Abdi-Jalebi, M.; Andaji-Garmaroudi, Z.; Cacovich, S.; Stavarakas, C.; Philippe, B.; Hutter, E. M.; Pearson, A. J.; Lilliu, S.; Savenije, T. J.; Richter, J. M. Maximizing and Stabilizing Luminescence from Halide Perovskites with Potassium Passivation. *Nature* **2018**, *555* (7697), 497–501.
- (17) Bag, S.; Durstock, M. F. Large Perovskite Grain Growth in Low Temperature Solution-Processed Planar p-i-n Solar Cells by Sodium Addition Large Perovskite Grain Growth in Low Temperature Solution-Processed Planar p-i-n Solar Cells by Sodium Addition. *ACS Appl. Mater. Interfaces* **2016**, *8* (8), 5053–5057.
- (18) Nie, W.; Tsai, H.; Asadpour, R.; Blancon, J.-C.; Neukirch, A. J.; Gupta, G.; Crochet, J. J.; Chhowalla, M.; Tretiak, S.; Alam, M. A.; et al. High-Efficiency Solution-Processed Perovskite Solar Cells with Millimeter-Scale Grains. *Science* **2015**, *347*, 522–525.
- (19) Deng, Y.; Dong, Q.; Bi, C.; Yuan, Y.; Huang, J. Air-Stable, Efficient Mixed-Cation Perovskite Solar Cells with Cu Electrode by Scalable Fabrication of Active Layer. *Adv. Energy Mater.* **2016**, *6* (11), 1600372.
- (20) Saliba, M.; Tan, K. W.; Sai, H.; Moore, D. T.; Scott, T.; Zhang, W.; Estroff, L. A.; Wiesner, U.; Snaith, H. J. Influence of Thermal Processing Protocol upon the Crystallization and Photovoltaic Performance of Organic-Inorganic Lead Trihalide Perovskites. *J. Phys. Chem. C* **2014**, *118* (30), 17171–17177.
- (21) Li, X.; Bi, D.; Yi, C.; Décoppet, J.-D.; Luo, J.; Zakeeruddin, S. M.; Hagfeldt, A.; Grätzel, M. A Vacuum Flash-Assisted Solution Process for High-Efficiency Large-Area Perovskite Solar Cells. *Science* **2016**, *353*, 58–62.
- (22) He, M.; Li, B.; Cui, X.; Jiang, B.; He, Y.; Chen, Y.; O’Neil, D.; Szymanski, P.; Ei-Sayed, M. A.; Huang, J.; et al. Meniscus-Assisted Solution Printing of Large-Grained Perovskite Films for High-Efficiency Solar Cells. *Nat. Commun.* **2017**, *8* (1–10), 16045.
- (23) Bag, S.; Deneault, J. R.; Durstock, M. F. Aerosol-Jet-Assisted Thin-Film Growth of $\text{CH}_3\text{NH}_3\text{PbI}_3$ Perovskites — A Means to Achieve High Quality, Defect-Free Films for Efficient Solar Cells. *Adv. Energy Mater.* **2017**, *7*, 1701151.
- (24) Wang, Z.; McMeekin, D. P.; Sakai, N.; van Reenen, S.; Wojciechowski, K.; Patel, J. B.; Johnston, M. B.; Snaith, H. J. Efficient and Air-Stable Mixed-Cation Lead Mixed-Halide Perovskite Solar Cells with n-Doped Organic Electron Extraction Layers. *Adv. Mater.* **2017**, *29* (1–8), 1604186.
- (25) Wang, Q.; Chen, B.; Liu, Y.; Deng, Y.; Bai, Y.; Dong, Q.; Huang, J. Scaling Behavior of Moisture-Induced Grain Degradation in Polycrystalline Hybrid Perovskite Thin Films. *Energy Environ. Sci.* **2017**, *10* (2), 516–522.
- (26) Dubey, A.; Kantack, N.; Adhikari, N.; Reza, K. M.; Venkatesan, S.; Kumar, M.; Khatiwada, D.; Seth Darling, S.; Qiao, Q. Room temperature, air crystallized perovskite film for high performance solar cells. *J. Mater. Chem. A* **2016**, *4*, 10231–10240.
- (27) Vicente, A. T.; Araújo, A.; Mendes, M. J.; Nunes, D.; Oliveira, M. J.; Sanchez-Sobrado, O.; Ferreira, M. P.; Águas, H.; Fortunato, E.; Martins, R. Multifunctional Cellulose-Paper for Light Harvesting and Smart Sensing Applications. *J. Mater. Chem. C* **2018**, *6* (13), 3143–3181.
- (28) Vicente, A. T.; Araújo, A.; Gaspar, D.; Santos, L.; Marques, A. C.; Mendes, M. J.; Pereira, L.; Fortunato, E.; Martins, R. *Optoelectronics and Bio Devices on Paper Powered by Solar Cells. Nanostructured Solar Cells*; Das, N., Ed.; IntechOpen: London, 2017.
- (29) Jung, B.; Kim, K.; Kim, W. Microwave-Assisted Solvent Vapor Annealing to Rapidly Achieve Enhanced Performance of Organic Photovoltaics. *J. Mater. Chem. A* **2014**, *2* (36), 15175–15180.
- (30) Ahn, J. H.; Lee, J. N.; Kim, Y. C.; Ahn, B. T. Microwave-Induced Low-Temperature Crystallization of Amorphous Si Thin Films. *Curr. Appl. Phys.* **2002**, *2* (2), 135–139.
- (31) Sun, J.; Wang, W.; Yue, Q. Review on Microwave-Matter Interaction Fundamentals and Efficient Microwave-Associated Heating Strategies. *Materials* **2016**, *9*, 231–256.
- (32) Hoz, A.; Diaz-Ortiz, A.; Moreno, A. Microwaves in organic synthesis. Thermal and non-thermal microwave Effects. *Chem. Soc. Rev.* **2005**, *34*, 164–178.
- (33) Mamun, A.; Chowdhury, A. H.; Chen, K.; et al. Rapid and Low Temperature Processing of Mesoporous and Nano-Crystalline TiO_2

Film Using Microwave Irradiation. *ACS Appl. Energy Mater.* **2018**, *1*, 6288–6294.

(34) Cao, Q.; Yang, S.; Gao, Q.; Lei, L.; Yu, Y.; Shao, J.; Liu, Y. Fast and Controllable Crystallization of Perovskite Films by Microwave Irradiation Process. *ACS Appl. Mater. Interfaces* **2016**, *8* (12), 7854–7861.

(35) Xu, J.; Hu, Z.; Jia, X.; Huang, L.; Huang, X.; Wang, L.; Wang, P.; Zhang, H.; Zhang, J.; Zhang, J.; Zhu, Y. A Rapid Annealing Technique for Efficient Perovskite Solar Cells Fabricated in Air Condition under High Humidity. *Org. Electron.* **2016**, *34*, 84–90.

(36) McMeekin, D. P.; Sadoughi, G.; Rehman, W.; Eperon, G. E.; Saliba, M.; Horantner, M. T.; Haghighirad, A.; Sakai, N.; Korte, L.; Rech, B.; et al. A Mixed-Cation Lead Halide Perovskite Absorber for Tandem Solar Cells. *Science* **2016**, *351* (6269), 151–155.

(37) Tan, W.; Bowring, A. R.; Meng, A. C.; McGehee, M. D.; McIntyre, P. C. Thermal Stability of Mixed Cation Metal Halide Perovskites in Air. *ACS Appl. Mater. Interfaces* **2018**, *10* (6), 5485–5491.

(38) Moehl, T.; Im, J. H.; Lee, Y. H.; Domanski, K.; Giordano, F.; Zakeeruddin, S. M.; Dar, M. I.; Heiniger, L.; Nazeeruddin, M. K.; et al. Park. Strong Photocurrent Amplification in Perovskite Solar Cells with a Porous TiO₂ Blocking Layer under Reverse Bias. *J. Phys. Chem. Lett.* **2014**, *5* (21), 3931–3936.

(39) Egorov, S. V.; Ereemeev, A. G.; Plotnikov, I. V.; Semenov, V. E.; Sorokin, A. A.; Zharova, N. A.; Bykov, Y. V. Edge Effect in Microwave Heating of Conductive Plates. *J. Phys. D: Appl. Phys.* **2006**, *39* (14), 3036–3041.

(40) Hoz, A.; Loupy, A. *Microwaves in Organic Synthesis*, 3th ed.; John Wiley & Sons: New York, 2013.

(41) Uchida, S.; Masahide, H.; Kawaraya, M. Flexible dye-sensitized solar cells by 28 GHz microwave irradiation. *J. Photochem. Photobiol., A* **2004**, *164*, 93–96.

(42) Ratke, L.; Voorhees, P. W. *Growth and Coarsening - Ostwald Ripening in Material Processing*; Springer-Verlag: Berlin, 2002.

(43) López, R.; Gómez, R. Band-Gap Energy Estimation from Diffuse Reflectance Measurements on Sol-Gel and Commercial TiO₂A Comparative Study. *J. Sol-Gel Sci. Technol.* **2012**, *61* (1), 1–7.

(44) Jeynes, C.; Colaux, J. L. Thin Film Depth Profiling by Ion Beam Analysis. *Analyst* **2016**, *141* (21), S944–S985.

(45) Johansson, S. A. E.; Campbell, J. L.; Malmqvist, K. G. *Particle-Induced X-Ray Emission Spectrometry (PIXE)*; Winefordner, J. D., Ed.; Wiley: New York, 1995.

(46) Chu, W. K. *Backscattering Spectrometry*, 1st ed.; Academic Press: San Diego, 1978.

(47) Barradas, N. P. Rutherford Backscattering Analysis of Thin Films and Superlattices with Roughness. *J. Phys. D: Appl. Phys.* **2001**, *34* (14), 2109–2116.

(48) Barreiros, M. A.; Alves, L. C.; Brites, M. J.; Corregidor, V. Depth Profile by Total IBA in Perovskite Active Layers for Solar Cells. *Nucl. Instrum. Methods Phys. Res., Sect. B* **2017**, *404*, 211–218.